

Quantitative analysis and temperature induced variations of moiré pattern in fiber-coupled imaging sensors

SALMAN KARBASI^{1,*}, ASHKAN ARIANPOUR¹, NOJAN MOTAMEDI¹, WILLIAM M. MELLETTE¹, AND JOSEPH E. FORD¹

¹Photonic Systems Integration Laboratory, Department of Electrical and Computer Engineering, University of California San Diego, La Jolla, CA 92093, USA

*Corresponding author: skarbasi@ucsd.edu

Compiled May 18, 2015

Imaging fiber bundles can map the curved image surface formed by some high-performance lenses onto flat focal plane detectors. Relative alignment between the focal plane array pixels and the quasiperiodic fiber bundle cores can impose an undesirable space variant moiré pattern, but this effect may be greatly reduced by flat-field calibration, provided the local responsivity is known. Here we demonstrate a stable metric for spatial analysis of the moiré pattern strength, and use it to quantify the effect of relative sensor and fiber bundle pitch, and that of the Bayer color filter. We measure the thermal dependence of the moiré pattern, and the achievable improvement by flat field calibration at different operating temperatures. We show that a flat-field calibration image at a desired operating temperature can be generated using linear interpolation between white images at several fixed temperatures, comparing the final image quality with an experimentally acquired image at the same temperature.

OCIS codes: (110.0110) Imaging systems, (060.2350) Fiber optics imaging, (110.2960) Image analysis, (110.4280) Noise in imaging systems.

<http://dx.doi.org/10.1364/ao.XX.XXXXXX>

1. INTRODUCTION

In monocentric fiber-coupled imagers, multicore imaging fiber bundles polished with a curved input face map a spherical image surface onto one or more focal planes [1–3]. This image transfer can cause aliasing (moiré patterns) to appear on the sensed image. Moiré effects can be eliminated by 4x to 8x oversampling of either the fiber bundle or image sensor, but the minimum practical pitch of both the optical fiber bundle and the sensor pixel are constrained by optical diffraction. The smallest commercially available focal plane pixels are 1.12 μm pitch, although larger (up to about 6 μm) pixels are typically used to achieve high image dynamic range [4]. Fiber bundles with numerical aperture of 1 and pitch more than about 2.2 μm can have high spatial contrast, but smaller pitches lead to coupling between fiber cores and low image contrast. This means that oversampling of either the fiber bundle or sensor intrinsically reduces the maximum information content of the image. Instead, the moiré pattern in images captured with comparable fiber and sensor pitches can best be minimized by analog pre-processing and digital post-processing to increase the image visual quality with minimal sacrifice of resolution or dynamic range.

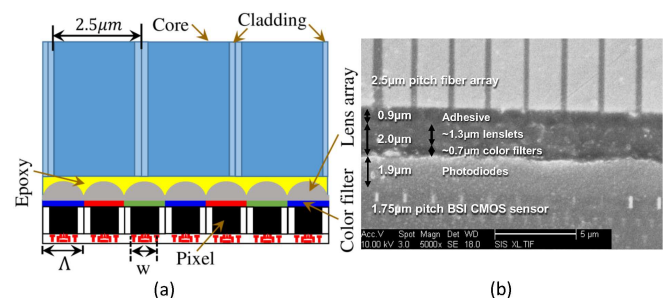


Fig. 1. (a) Cross-sectional schematic of a fiber bundle with a pitch size of $2.5\mu\text{m} \times 2.5\mu\text{m}$ attached to a color focal plane array with a pitch size of $\Lambda \times \Lambda$, (b) scanning electron microscope (SEM) image of a cross-sectioned fiber-coupled back-side illuminated CMOS focal plane with $\Lambda = 1.75\mu\text{m}$.

Analog signal preprocessing is done by the physical structure of the fiber-coupled sensor, including the choice of fiber structure and integration method. For example, rotating the axis of the fiber lattice with respect to the axis of the focal plane [5] increases the spatial frequency of the raw moiré pattern, which tends to reduce the visual impact. A cross-sectional schematic and scanning electron microscope image of a fiber-coupled sensor are shown in Figs. 1(a) and 1(b), respectively.

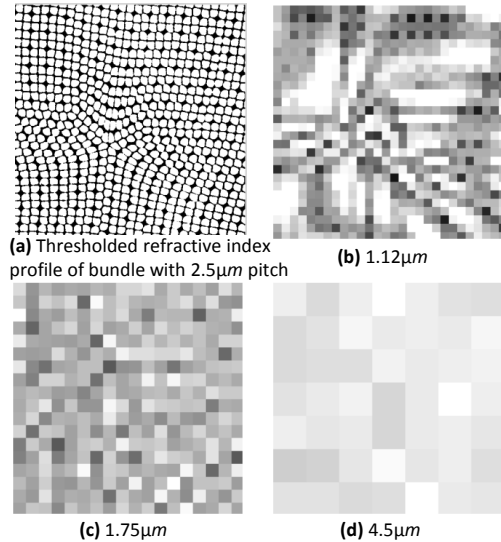


Fig. 2. (a) Thresholded refractive index profile of the SCHOTT 24AS fiber bundle in a $62.5\mu\text{m} \times 62.5\mu\text{m}$ region, and numerically generated moiré degraded "white" images by sampling this profile by an individual color channel with the pitch of (b) $1.12\mu\text{m}$, (c) $1.75\mu\text{m}$, and (d) $4.5\mu\text{m}$.

In Fig. 2 (a), a thresholded refractive index profile of a SCHOTT 24AS fiber bundle with a pitch of $2.5\mu\text{m}$ and numerical aperture of 1 is numerically sampled by an individual color channel of focal planes with 98% active area fill factor and a pitch (Λ) of $1.12\mu\text{m}$, $1.75\mu\text{m}$ and $4.5\mu\text{m}$, in Figs. 2(b-d), respectively. The sampled images of the refractive index profile of the fiber resemble white images captured with a fiber-coupled sensor. The sensor pitches (Λ) used in the numerical simulations in Fig. 2 are those of the following commercially available back-side illuminated CMOS focal planes: the 13Mpixel $1.12\mu\text{m}$ pitch OmniVision OV13850, the 5Mpixel $1.75\mu\text{m}$ pitch OmniVision OV5653, and the 25 Mpixel $4.5\mu\text{m}$ pitch On Semiconductor VITA 25K. The generated gray scale images show the modulation for a $1.12\mu\text{m}$ pitch sensor is deeper than that for $1.75\mu\text{m}$ or $4.5\mu\text{m}$ pitch sensors. Increasing the fiber-sensor distance via a thicker adhesive seam will also reduce moiré artifacts by spreading the emitted light from the fiber bundle. However, a larger pitch sensor reduces the resolution of the fiber-coupled system to that of the sensor pitch, and increasing fiber-sensor separation reduces spatial resolution due to blurring. The challenge is to reduce moiré without compromising the resolution.

In this work, we focus on a sensor pitch of $1.12\mu\text{m}$ because it results in the strongest moiré pattern when using a $2.5\mu\text{m}$ SCHOTT 24AS fiber bundle [6]. In addition, the axis of the fiber bundle lattice in most regions is purposely only rotated by 2° with respect to the axis of the sensor pixels, and the fiber-sensor distance is purposely minimized. These fabrication factors are the worse-case for the analog preprocessing of moiré and allow us to better assess the capabilities of digital post-processing techniques.

Digital post-processing by flat-field calibration can dramatically reduce the moiré pattern in the final images [7–9]. Here a white image taken with the system is used for pixel-wise division of subsequent images, regardless of the scene. This method has been used to reduce both deterministic image defects and moiré patterns for fiber-coupled monocentric imagers [9]. However, these initial experiments used white calibration images acquired at the same temperature as the scene images. Moiré patterns are strongly dependent on the relative positions of the fiber cores and sensor pixels. Because the coefficient of thermal expansion (CTE) of the glass fiber bundle ($6.8\text{ppm}/^\circ\text{C}$, [10]) does not match that of the silicon CMOS sensor ($3.6\text{ppm}/^\circ\text{C}$, [11]), we expect the moiré pattern to change with temperature.

In this paper we explore the impact of thermally induced variations of the moiré pattern strength in the calibration of the images taken with fiber-coupled sensors, and show the method can be used over a large range of operating temperatures.

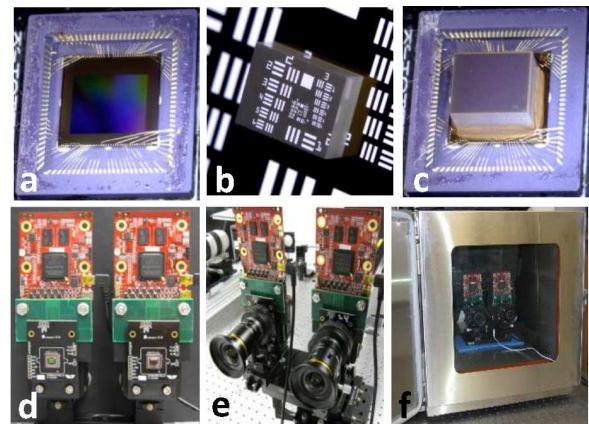
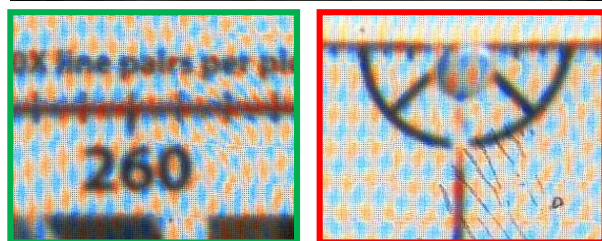
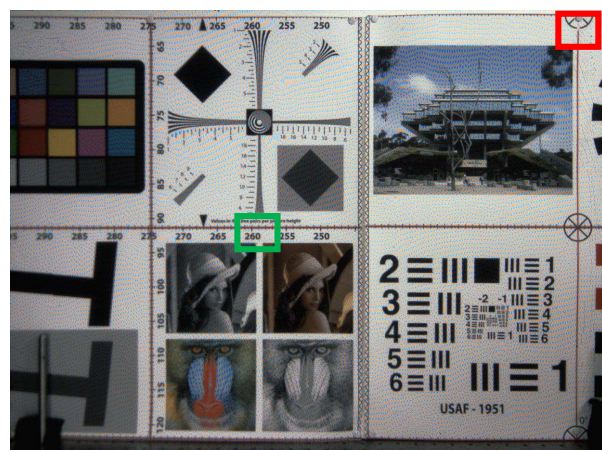


Fig. 3. (a) Bare OV13850 sensor without cover glass, (b) machined fiber-bundle on USAF test chart, (c) fiber-coupled sensor, (d) bare and fiber-coupled sensors connected to the electronic drives, (e) integrating the telecentric lenses with the sensors, and (f) imaging system in the oven looking outside through the glass window.

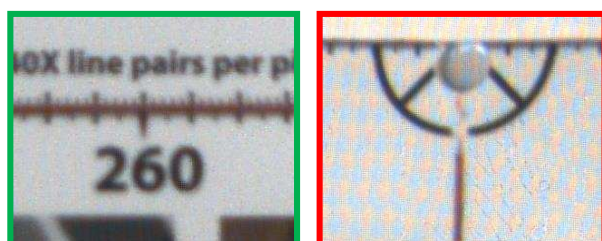
2. ASSEMBLY AND FLAT-FIELD CALIBRATION

To assemble a fiber-coupled sensor, the sensor's cover glass is removed, as shown in Fig. 3(a), and a $4.9\text{mm} \times 3.73\text{mm}$ machined fiber bundle with a length of 2.63mm (Fig. 3(b)) is bonded to the bare sensor's surface using UV-cured Norland NOA72 adhesive (Fig. 3(c)). We used SCHOTT 24AS imaging fiber bundles (Fig. 2(a)) with a pitch size of $2.5\mu\text{m}$, 80% core-pitch duty cycle, and a numerical aperture of 1 [6]. During the stack-and-draw manufacturing process, fiber orientations in the lattice can vary at different regions in the bundle. This results in variations in the moiré pattern at different regions of the images obtained with fiber-coupled sensor, as seen in the numerical analysis in Fig. 2. The assembled bare and fiber-coupled sensors are shown in a testbed in Fig. 3(d). The setup with added telecentric lenses in Fig. 3(e) is placed in an oven looking outside through the glass window, Fig. 3(f), in order to control the temperature of the bare and fiber-coupled imagers simultaneously.

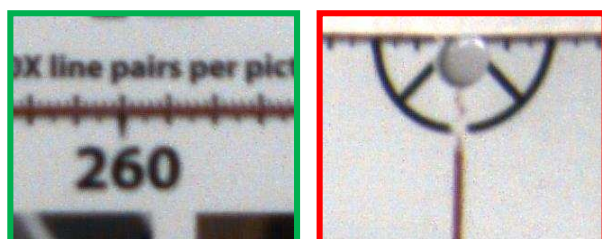
Fig. 4(a) shows an example of a 13Mpixel image acquired with the color fiber-coupled sensor with $1.12\mu\text{m}$ pixels and a telecentric flat-focus lens (Kowa LM5JC10M, 5mm focal length, F/2) at 23°C . The color image is generated from the Bayer color



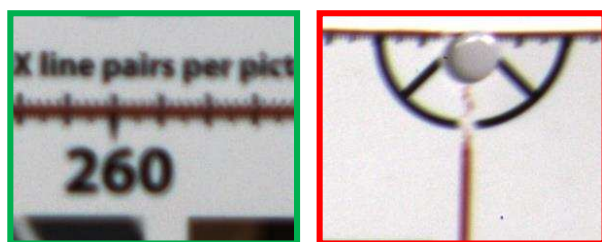
(a) Uncalibrated fiber-coupled image acquired with system at 23°C



(b) Calibrated using a 27° mismatched flat field image acquired at 50°C



(c) Calibrated using a temperature-matched flat-field image acquired at 23°C



(d) Image acquired by a bare focal plane sensor (no fiber bundle)

Fig. 4. (a) Un-calibrated image from fiber-coupled sensor, (b) calibrated image at 23°C using a flat-field image at 50°C, (c) calibrated image at 23°C using a flat-field image at 23°C, and (d) image taken with bare sensor. In all the images, telecentric lenses (Kowa LM5JC10M) with 5mm focal length and F/2 are used. The image sensor is OV13850 with a pitch size of 1.12 μ m. Bayer CFA is interpolated using bilinear method. In (b), (c) and (d) Bayer interpolation was performed on the calibrated raw images.

filter array (CFA) raw image data using bilinear interpolation. The zoomed-in images in Fig. 4(a) show strong moiré artifacts which originated from the moiré in the raw gray-scale image and were amplified by CFA interpolation. The observed moiré pattern can be significantly reduced through flat-field calibration of the raw image using an image of a white uniformly illuminated scene. The raw images used in the flat-field calibration process are first calibrated to remove fixed pattern sensor noise associated with dark current by subtracting the corresponding dark images. In the temperature ranges of our experiments, thermal variations of the dark image were insignificant.

We take two sets of 10 flat-field images at temperatures of 23°C and 50°C. The averaged flat-field of each set is used for calibration of the image in Fig. 4(a). The calibrated images using the flat-fields at 23°C and 50°C are shown in Figs. 4(b) and (c), respectively. The flat-field calibration using a white image at a different temperature (Fig. 4(b)) still significantly reduces the moiré variations compared with an uncalibrated image (Fig. 4(a)). The calibrated image in Fig. 4(b) shows some residual moiré variation in the region close to the edge of the image compared with the center of the scene. The same temperature calibration in Fig. 4(c) dramatically reduces the moiré from both the center and edge of the image and is comparable to the bare sensor image in Fig. 4(d). Although the moiré is significantly reduced in the calibrated images even using different temperature flat-fields, the results show for an optimum flat-field calibration the white image needs to be acquired at the operating temperature of the imager. The highest temperature for acquiring the images in Fig. 4 is limited by the maximum safe operating temperature for the telecentric lenses which is 50°C.

To investigate the impact of differential thermal expansion of the fiber bundle and the sensor on moiré pattern over a larger temperature range, we removed the imaging lenses from the system and directly illuminated the setup in Fig. 3(d) by a collimated white light source placed outside of the oven. The temperature of the sensors can be safely increased to around 70°C. Although this method limits our acquired scenes to white images, here we assume (based on a range of image observations) that the moiré pattern strength does not depend on specific scene features. In the next section, we develop a metric to analyze moiré strength in raw white images to study temperature induced variation of moiré pattern.

3. QUANTITATIVE ANALYSIS OF MOIRÉ PATTERN IN WHITE IMAGES

Subjective evaluation of moiré pattern is variable, and can be influenced by additional aliasing caused by the sampling of the display medium (e.g., computer monitor resolution). Here, we develop a metric for raw image moiré strength that is independent of display format and can be used for objective evaluation of local regions of a white image. Methods such as mean squared error (MSE), peak signal to noise ratio (PSNR), and structural similarity index (SSIM) have been used extensively for objective image quality evaluation [12]. These metrics require a reference image to assess the differences (in MSE and PSNR) or similarities (in SSIM) between the two images. In moiré strength analysis using SSIM, MSE and PSNR, the similarities and differences of the white images taken with the fiber-coupled sensor can be compared to a theoretical white image at the same average intensity level. However, we found that MSE, PSNR, and SSIM are sensitive to the variations in the pixel in-

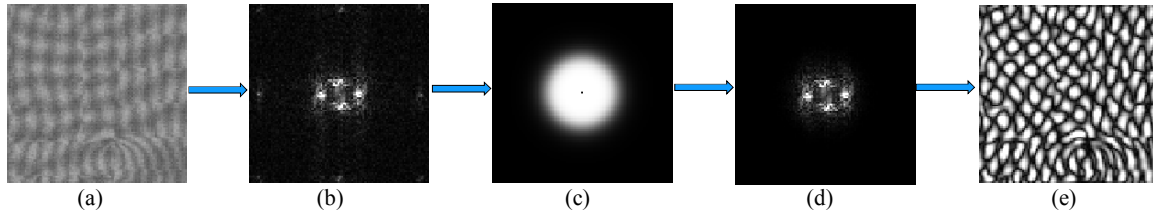


Fig. 5. Filtering and DC-removal procedure on a 100×100 pixel raw gray scale image region. (a) spatial image, (b) modulus of Fourier transform, (c) low-pass filter with zero DC, (d) filtered image in spectral domain, and (e) modulus of inverse Fourier transform.

tensities caused by sensor noise, resulting in artifacts in evaluation of moiré pattern in the images. To address this, we develop a method to track spatial variations of the moiré pattern using a windowed Fourier transform. First, an image is segmented into periodic regions, each large enough to contain several periods of the moiré. The image in each window is filtered using a 4th order low-pass Butterworth filter, and the DC value is removed, as shown in Figs. 5(a-e). The cut-off frequency of the low-pass filter is chosen to be large enough to retain the low frequency moiré variations in the original image, but to remove high frequency sensor noise. Samples of the spatial images and their filtered spectral information in 100×100 pixel windows at different regions of the white image are shown in Figs. 6(a-d). For visual display of the spatial variation a moiré “energy map” of the whole image can then be calculated by integrating the squared spectral signal in each window, as formulated in Eq. 1, where $\psi_{i,j}$ is the energy in the (i^{th} , j^{th}) patch and $s_{i,j}$ is the filtered $M \times N$ signal patch.

$$\psi_{i,j} = \sum_{n=1}^N \sum_{m=1}^M s_{i,j}^2(n, m) \quad (1)$$

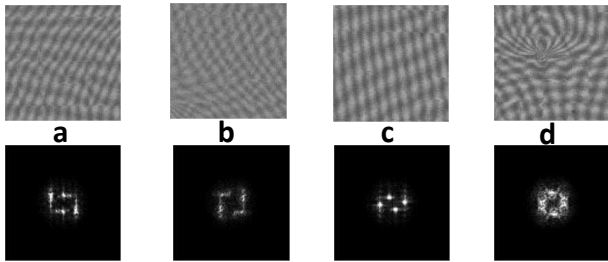


Fig. 6. (a-d) Top row are raw 100×100 pixel patches at different spatial locations of the green² channel from the fiber-coupled sensor (OV13850) at 22°C. The bottom row shows the modulus of the spectral images on the top row. In the spectral images, the DC value is removed and a 4th order Butterworth low-pass filter with a radius of 20 pixels is applied.

Here the local patches are chosen to be 100×100 pixels, to contain several periods of moiré and still locally track the variations in the moiré pattern. The radius of the low-pass filter is 20 pixels in the spectral domain. The spectral domain analysis presented here mitigates the dependence of the moiré pattern evaluation on the high frequency sensor noise as well as the background intensity of the images, and only considers the moiré oscillations. Because high frequency noise has been removed, the signal fidelity metrics such as SSIM, MSE, and PSNR can be effectively used to compare the energy maps, as will be shown in the last section.

4. APPLYING THE METRIC ON RAW UN-CALIBRATED IMAGES

For these measurements, we used two color BSI CMOS sensors, the $1.75 \mu\text{m}$ pitch OV5653 and the $1.12 \mu\text{m}$ pitch OV13850, which include microlenses and Bayer color filters. We also tested a monochrome $1.12 \mu\text{m}$ pitch OV13351 sensor, which is identical to the OV13850 other than the omission of both microlenses and color filters. This brings the fiber bundle into the closest possible contact (measured by SEM cross sections to be as little as $1.8 \mu\text{m}$) with the silicon chip and active photosensitive volume. Fiber-coupled sensors were covered by plane-plane polished $2.5 \mu\text{m}$ pitch fiber bundles.

To record the white images, the focal planes shown in Fig. 3(d) were directly illuminated (without lenses) by a collimated and intensity-controlled white LED light source. The raw images acquired for all the sensors are taken to have the same average gray-scale intensity level by adjusting the individual color channel gain of the sensors to compensate for transmission efficiency of the color filters in the color sensors. For comparison of the moiré pattern in the fiber-coupled sensors with different pitches, we use an individual color channel in the color sensors (OV13850 and OV5653) and down sampled the image of the monochrome sensor (OV13351) to resemble the pattern of an individual Bayer channel. The assembly of the three fiber-coupled sensors is similar to that of the color sensor with the pitch of $1.12 \mu\text{m}$, as described in the previous section. Using the individual channels to study the moiré pattern on the illumination spectrum and transmission efficiencies of the fiber-bundle and different color filters. The green² channel white images obtained with the fiber-coupled sensors, and corresponding energy map using Eq. 1 are shown in Fig. 7. The observed moiré pattern in the white image of the $1.75 \mu\text{m}$ color sensor, Fig. 7(a), is much less pronounced compared with those of the color and monochrome sensors with $1.12 \mu\text{m}$ pitch, shown in Figs. 7(b) and 7(c), respectively. This observation matches the prediction in Fig. 2. The moiré strength in the spatial images acquired with the $1.75 \mu\text{m}$ color sensor is visibly less than that in the color and monochrome $1.12 \mu\text{m}$ pitch sensors, but there is no immediately visible difference between the $1.12 \mu\text{m}$ monochrome and color sensor images. The energy map metric clarifies the differences between the $1.12 \mu\text{m}$ pitch color and monochrome fiber coupled sensors. Stronger moiré artifacts in the monochrome sensor are due to a smaller separation between the fiber-bundle and the sensor. It should be noted that despite the lack of microlenses for the monochrome sensor, the effective fill-fractions of the pixel active areas of both color and monochrome $1.12 \mu\text{m}$ sensors are similar because the refractive index of the epoxy used to attach the bundles to the sensors is matched with that of the lens array in the color sensor, which eliminates the lenslet focusing power.

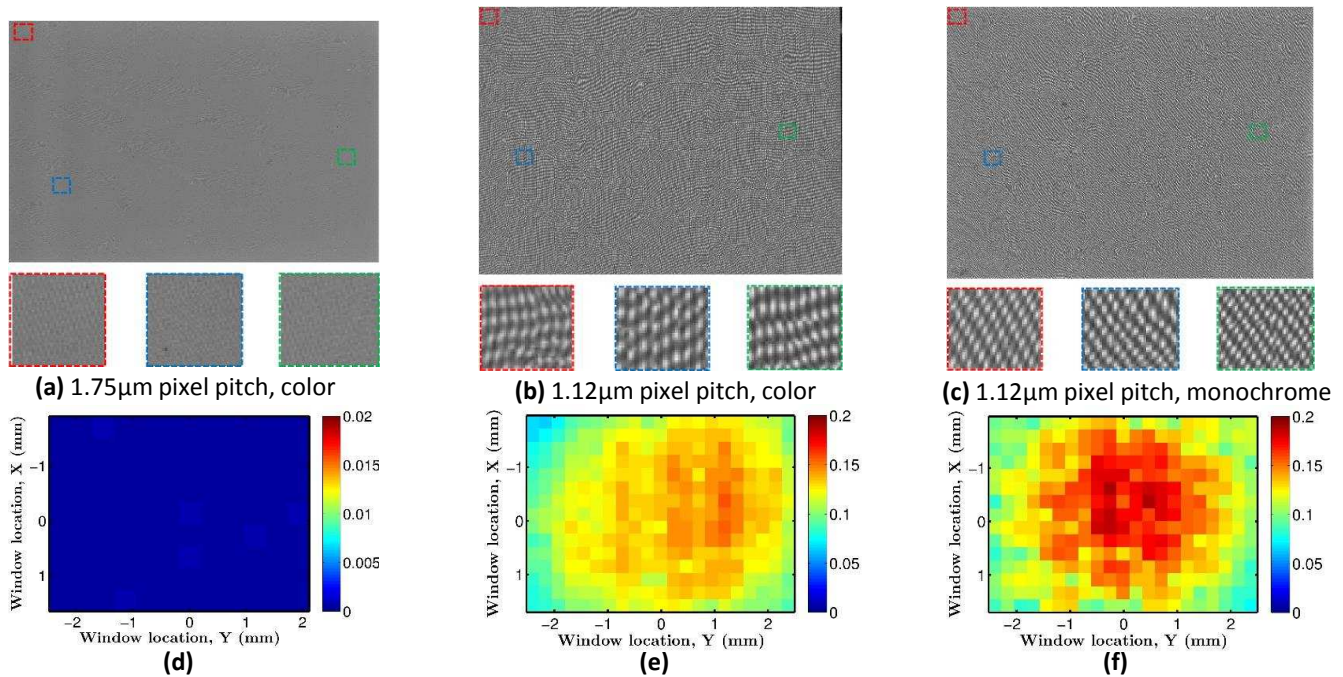


Fig. 7. Green² channel of a white image obtained with $2.5\mu\text{m}$ pitch fiber coupling of (a) $1.75\mu\text{m}$ pitch color (OV5653), and (b) $1.12\mu\text{m}$ color (OV13850) sensors. (c) The down-sampled image to the size of an individual channel of the white image acquired with $1.12\mu\text{m}$ pitch monochrome (OV13351) fiber-coupled sensor. (d) Energy map of (a), (e) energy map of (b), and (f) energy map of (c). Size of the images are 972×1296 pixels in (a) and 1568×2112 pixels in (b) and (c).

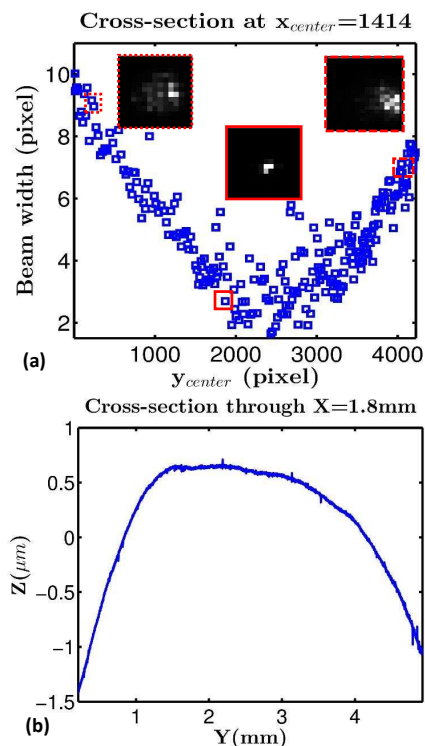


Fig. 8. (a) Width of the detected beam by the monochrome fiber-coupled sensor with pixel pitch of $1.12\mu\text{m}$ (OV13351) versus the center of the beam (y_{center}). The input beam is scanned along a line close to the center of sensor ($x_{center} = 1414$), by translating the fiber-coupled sensor. The dimensions of each image used in this calculation are 3136×4224 pixels. The intensity profiles of the detected beams at $y_{center} = 71, 1986,$ and 4218 are shown at subfigures in (a). (b) The height (Z) versus the length (Y) of bare OV13351 sensor's surface across the center in X direction. The profile is measured using the Wyko NTT1100 optical profiling system. The image area of the sensor is $4.81\text{mm} \times 3.68\text{mm}$ ($Y \times X$).

5. SPATIAL NON-UNIFORMITIES IN MOIRÉ ENERGY

In the previous section, the moiré energy maps of the $1.12\mu\text{m}$ pixel pitch color and monochrome fiber-coupled sensors in Figs. 7(e) and 7(f) showed a smaller energy at the edges of the images compared to the central region. This would be unexpected, if the sensor, fiber bundle, and adhesive seam were uniform over the sensor area.

As a first step in characterizing the low energy regions around the edges of the energy map, we measured the impulse response of the monochrome fiber-coupled sensor using a 611.9nm He-Ne laser. Collimated laser light was focused using a $20\times$ ($\text{NA}=0.42$) microscope objective and launched into the fiber bundle. The input beam is scanned at 250 points along a line in the longer dimension (' Y ') of the monochrome fiber-coupled sensor. We used the first- and second-moment methods in Ref. [13], respectively to calculate the centroid and beam width for each image acquired along the line scan. The absence of color filters in the $1.12\mu\text{m}$ pitch monochrome sensor makes our observations in this section independent of the transmission efficiency of the color filter. The measured width of the detected beam versus the location of the beam presented in Fig. 8(a) shows a wider impulse response at the regions away from the center of the image. Samples of the detected intensity profiles at different regions along the line are shown in the sub-figures.

We used the Wyko NTT1100 optical profiling system to identify the presence of any curvature in a bare monochrome sensor (OV13351) similar to that used in the fiber-coupled sensor. The cross section of the measured profile of the bare monochrome sensor along the center is shown in Fig. 8(b). It should be noted that the image area of the monochrome sensor is $4.81\text{mm} \times 3.68\text{mm}$ and the cross section shown in Fig. 8(b) covers the whole length of the sensor. The measured profile shows a depth of $1.5\mu\text{m}$ to $2\mu\text{m}$ in the regions close to the bound-

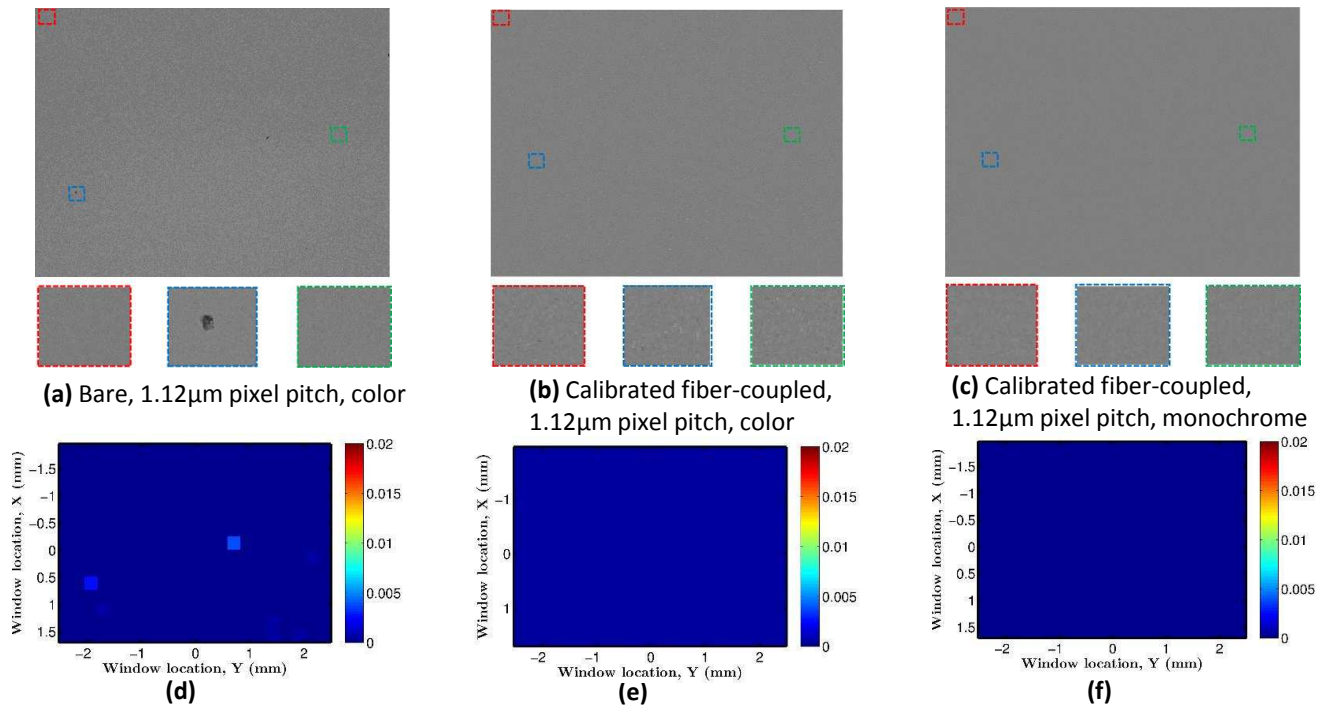


Fig. 9. Green² channel of a white image obtained with (a) bare color sensor (OV13850), (b) calibrated image with fiber-coupled color sensor (OV13850) at the same temperature, and (c) calibrated image of monochrome fiber-coupled sensor (OV13351) at the same temperature. (d) energy map of (a), (e) energy map of (b) and (f) energy map of (c). The sensor pixel size is $1.12\mu\text{m} \times 1.12\mu\text{m}$. Size of the images in (a-c) is 1568×2112 .

aries of the sensor. The resulting thicker adhesive line and the beam expansion explains the wider impulse response in these regions. The increased spatial dispersion of the light emitted from the rear fiber face reduces moiré strength in the regions close to the boundaries of the monochrome fiber-coupled sensor in Fig. 7(c).

The same effect describes the lower energy of moiré near the edges of images obtained with the fiber-coupled $1.12\mu\text{m}$ pitch color sensor. The impact of curvature in the fiber-coupled color sensor is expected to be less due to a larger distance between the fiber bundle and the sensor.

6. FLAT-FIELD CALIBRATION OF WHITE IMAGES

The images taken with the $1.12\mu\text{m}$ pitch sensor at a room temperature of 22°C presented previously in Figs. 7(b) and 7(c) contain strong moiré patterns compared with the uniform green² channel white image of the bare sensor (OV13850) shown in Fig. 9(a). White images taken with the $1.12\mu\text{m}$ pitch color and monochrome fiber-coupled sensors which have been calibrated with the flat-field calibration method are shown in Figs. 9(b) and 9(c), respectively. The white flat-field images used for calibration of the fiber-coupled sensors were taken at the same temperature, and only 10 seconds later than the original images in each case. The observed random noise pattern in the raw calibrated images, shown in Figs. 9(b) and 9(c), are on the order of variations in the bare-sensor image shown in Fig. 9(a). The energy maps of the images in Figs. 9(a-c) are calculated using Eq. 1 in Figs. 9(d-f), respectively.

The energy map of the bare sensor in Fig. 9(d) contains two very small non-uniform regions that are caused by dust particles observed on the sensor surface, which can be seen in Fig. 9(a). The energy maps of the calibrated images in Figs. 9(e) and 9(f) show an effective removal of the moiré compared with the energy map of the uncalibrated images in Figs. 7(e) and 7(f).

Ref. [9] performed flat-field calibration without monitoring or controlling sensor temperature. In the next section, we use our energy metric to investigate the impact of temperature variations on the flat-field calibration.

7. CALIBRATION OF FIBER-COUPLED MONOCHROME AND COLOR SENSORS AT DIFFERENT TEMPERATURES

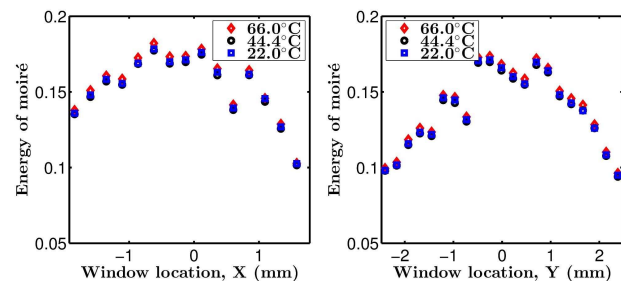


Fig. 10. Cross sections of individual channel energy maps of OV13351 fiber-coupled sensor in 'X' and 'Y' directions for different temperatures.

In the previous section, it was shown that the calibration of white images taken at room temperature using the flat-fields taken at the same temperature results in effective removal of the moiré pattern for the fiber-coupled monochrome and color sensors. A set of images at temperatures ranging from 22° to 66°C were taken with the fiber-coupled OV13351 (monochrome) and OV13850 (color) sensors through the window of a temperature-stabilized oven. Each time the temperature was changed, images were acquired after waiting one hour to allow the system to reach thermal equilibrium. The white images were generated by direct illumination of the sensors by a collimated white LED

light source. We calibrated white images taken above room temperature using flat-field images taken at the same and different temperatures. We waited 10 seconds between capturing the white image and the flat-field at the same temperature. There is a longer time delay between capturing the white image and the flat-field when they are taken at different temperatures. Energy map cross-sections for the monochrome sensor at different temperatures show a slight increase in the energy of moiré at higher temperatures (see Fig. 10). These minimal variations can still result in strong fluctuations in a calibrated image because of the division operation inherent to the flat-field calibration process. The energy maps of calibrated white images at 66°C using flat-fields obtained at 66°C, 44°C, and 22°C are shown in Figs. 11(a-c), respectively. Figure 11(a) shows that the calibration of a white image at 66°C using the same temperature flat-field results in a uniform energy map similar to the room-temperature calibrated image shown in Fig. 9(f). On the other hand, calibration of the 66°C image using flat-fields at different temperatures results in non-uniformities in the calibrated images, as shown in the energy maps in Figs. 11(b) and 11(c).

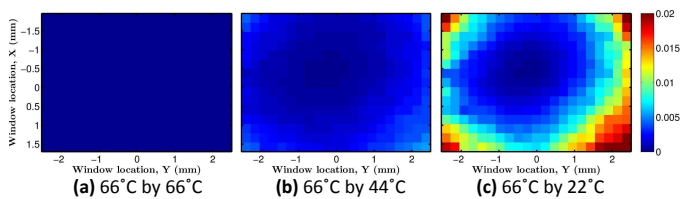


Fig. 11. Energy maps of down-sampled images with the monochrome fiber-coupled sensor (OV13351) at 66°C using flat-fields at (a) 66°C, (b) 44°C and (c) 22°C. The flat-field at 66°C is acquired 10s after the original image.

The same calibration process is performed using images taken with the color fiber-coupled sensor. The energy maps of the calibrated images taken at 66°C using flat-fields at different temperatures for the green² channel of the raw image acquired with the color fiber-coupled sensor are shown in Figs. 12(a-c). We observe similar trends for the different color channels of the color fiber-coupled sensor as we do with the monochrome sensor. We see larger moiré energy at the regions close to the boundaries of the calibrated images when using different temperature flat-fields. A similar trend is observed for the other channels.

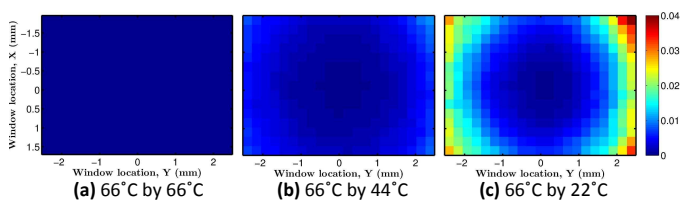


Fig. 12. Calibrated energy maps of green² channel obtained with the color fiber-coupled sensor (OV13850) at 66°C using the flat-fields at (a) 66°C, (b) 44°C, and (c) 22°C.

The results in this section show that the flat-field calibration can significantly reduce the moiré pattern in the fiber-coupled images, as long as the flat-field images are taken at the working temperature of the system. The calibration of images using flat-fields at very different temperatures can result in artifacts in the regions close to the boundaries of the calibrated images because of the difference between the CTE of the glass fiber and silicon sensor [14]. It should be noted that the observed non-uniformities at the regions close to the boundaries of the cali-

brated images using different temperature flat-fields are similar whether the flat-field temperature is lower or higher than the original image. It should also be noted that calibrating white images taken with the bare sensor using flat-fields at different temperatures does not result in any artifacts in the calibrated image.

8. GENERATION OF FLAT-FIELD AT A DESIRED TEMPERATURE

We found that thermal hysteresis of the fiber-coupled sensor was insignificant, implying that white images can be used for calibration of images taken later at the same temperature. A straightforward method to remove the moiré pattern in images taken at different temperatures is to store a look up table of white images taken at various temperatures, but in practice only a limited number of white images can be recorded and kept available. A previously proposed method to overcome this limitation for flat-field calibration of X-ray images uses a polynomial fit on several flat-field images at known conditions to generate the flat-field images for an unknown condition [15]. We used a similar procedure to generate a flat-field image at a desired temperature using white images at several known temperatures.

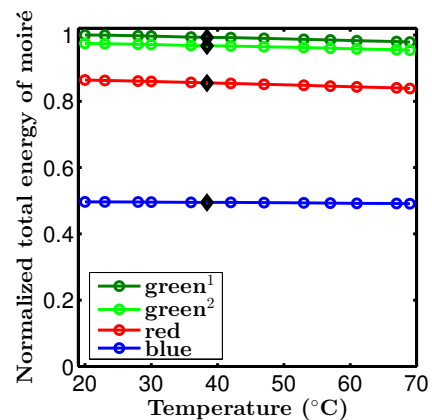


Fig. 13. Total energy of moiré versus temperature for all the channels (green¹, green², red and blue). The black diamond markers at 38.4°C show the total energy of moiré at different channels of the interpolated image at 38.4°C.

We calculate the total energy of each color channel by integrating over the energy map and use this single value as a metric to identify the trend of the moiré energy versus temperature. The variations of the total moiré energy in the white images versus temperature for different channels are shown in Fig. 13. The variations in the total moiré energy of the white images versus temperature is very small, but using a white image at a different temperature for calibration can still result in artifacts in the corrected images (as discussed in sections 2 and 6). Due to the linear behavior of the moiré energy, we choose to implement a linear interpolation method for generating white images at arbitrary temperatures. As an example, we applied the interpolation process on the individual pixels of white images at known temperatures to calculate a white image at the temperature of 38.4°C. The total moiré energy for each color channel of the interpolated image at 38.4°C is plotted in black diamond markers in Fig. 13. In Figs. 14(a) and 14(d), the green² channel energy map of the interpolated white image at 38.4°C is compared with that of an experimentally obtained image at

the same temperature. The peak signal to noise ratio (PSNR) for red, blue, green¹ and green² channels of the interpolated and experimental images are 73.7dB, 77.4dB, 70.94 dB, and 70.0dB, respectively. The calculated structural similarity index (SSIM) for the energy maps of all channels in the interpolated and experimentally acquired images are higher than 0.999. Comparing the energy maps using PSNR and SSIM as well as the total energy metric shows very good agreement between the moiré energy of the linearly interpolated white image and that of the experimentally acquired image at the same temperature (see Fig. 14). Calibration of the experimentally obtained image at 38.4°C using the interpolated image results in a uniform image shown in Fig. 14(c).

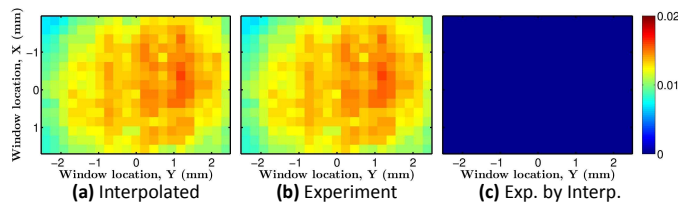


Fig. 14. Green² channel energy map of fiber-coupled sensor (OV13850) at 38.4°C using (a) interpolated image and (b) experimental data at the same temperature. The axes of the surface plots show the actual dimensions of the sensor. Peak signal to noise ratio (PSNR) and structural similarity index (SSIM) of (a) and (b) energy maps are 70.94dB and 0.999, respectively. (c) Green² channel energy map of the experimentally acquired image after calibration using the numerically interpolated image, demonstrating that effective thermal compensation can be achieved via extrapolation from a single stored image data field.

9. CONCLUSION

In summary, we have presented experimental characterization of fiber-coupled image moiré effects to show that a larger pixel size of the sensor or a larger distance between the fiber bundle and the sensor results in less variations of the moiré pattern (along with less image spatial resolution). We described a technique based on spectral domain analysis to quantitatively analyze moiré patterns in fiber-coupled sensor images and showed that this method can quantify moiré pattern variations that may not be visible in spatial domain images due to random sensor noise and DC image intensity. We used this energy map metric to quantify the residual moiré in images calibrated using flat-fields at different temperatures. We showed that for a stable flat-field calibration, the white images should be taken at the operating temperature of the fiber-coupled sensor, but also that interpolation between multiple white images at known temperatures can be effectively used for the real-time generation of white flat-field images at arbitrary operating temperatures of the fiber-coupled sensor.

10. ACKNOWLEDGMENTS

This work was supported by funding from Google ATAP, and from the DARPA "SCENICC" program, contract W911NF-11-C-0210. Special thanks to Sean Stetson and Andrey Yatsunenko at Google for their help in obtaining and interfacing to the 1.12 μ m focal plane sensor.

REFERENCES

1. T. S. Axelrod, N. J. Colella, and A. G. Ledebuhr, "The wide-field-of-view camera," *Energy and Technology Review*, Lawrence Livermore National Laboratory, pp. 1–12, Dec. 1988.
2. J. Ford, I. Stamenov, S. J. Olivas, G. Schuster, N. Motamedi, I. P. Agurok, R. Stack, A. Johnson, and R. Morrison, "Fiber-coupled monocentric lens imaging," in *Imaging and Applied Optics*, OSA Technical Digest (online) (Optical Society of America, 2013), paper CW4C.2.
3. I. Stamenov, A. Arianpour, S. J. Olivas, I. P. Agurok, A. R. Johnson, R. A. Stack, R. L. Morrison, and J. E. Ford, "Panoramic monocentric imaging using fiber-coupled focal planes," *Opt. Express* **22**, 31708–31721 (2014).
4. A. S. Tremsin, O. H. W. Siegmund, M. A. Gummin, P. N. Jelinsky, and J. M. Stock, "Electronic and optical moiré interference with microchannel plates: artifacts and benefits," *Appl. Opt.* **38**, 2240–2248 (1999).
5. G. M. Lawrence, "Hex-square moiré patterns in imagers using microchannel plates," *Appl. Opt.* **28**, 4337–4343 (1989).
6. "An Introduction to Fiber Optic Imaging" download available at <http://www.us.schott.com/lightingimaging/english/download/fo.book.pdf>.
7. J. A. Seibert, J. M. Boone and K. K. Lindfors, "Flat-field correction technique for digital detectors", *Proc. SPIE* **3336**, Medical Imaging 1998: Physics of Medical Imaging **348**, 348–354 (1998).
8. R. G. van Silfhout and A. S. Kachatkou, "Fibre-optic coupling to high resolution CCD and CMOS image sensor," *Nucl. Instrum. Methods* **597**, 266–269 (2008).
9. S. J. Olivas, A. Arianpour, I. Stamenov, R. Morrison, R. Stack, A. Johnson, I. P. Agurok, and J. E. Ford, "Image processing for cameras with fiber bundle image relay," *Appl. Opt.* **54**, 1124–1137 (2015).
10. J. J. Hancock, The design, fabrication, and calibration of a fiber filter spectrometer, Ph.D. Thesis (University of Arizona, 2012); see also product datasheets posted on SCHOTT Fiber Optics website, "Schott Fiber Optic Faceplates"(faceplates-us-march2011.pdf) and "Schott Fused Imaging Fiber Tapers" (Tapers-US-October2011.pdf).
11. W. M. Yim and R. J. Paff, "Thermal expansion of AlN, sapphire, and silicon," *J. Appl. Phys.* **45**, 1456–1457 (1974).
12. Z. Wang and A. C. Bovik, "Mean squared error: love it or live it?," *IEEE Sig. Process. Mag.* **26**, 98–117 (2009).
13. A. Mafi and J. V. Moloney, "Beam quality of photonic crystal fibers" *IEEE J. LightW. Technol.*, **23**, 2267–2270 (2005).
14. W. Zhang, D. Wu, B. Su, S. A. Hareb, Y. C. Lee, and B. Pat Masterson, "The effect of underfill epoxy on warpage in flip-chip assemblies" *IEEE T. Compon. Pack T.* **21**, 323–329 (1998).
15. A. L. C. Kwan, J. A. Seibert, and J. M. Boone, "An improved method for a flat-field correction of flat panel X-ray detector," *Med. Phys.* **33**, 391–393 (2006).